Chapter 2

Ion-Nanoscale Matter Interactions

Elmuez A. Dawi

Additional information is available at the end of the chapter

http://dx.doi.org/10.5772/intechopen.76862

Abstract

Irradiation of spherical gold (Au) nanoparticles confined within a silica matrix with swift heavy ions induces their shaping into prolate nanorods along the beam direction. In this review, spherical colloidal Au nanoparticles with a diameter in the range of 15–30 nm (±3 nm) are irradiated at normal incidence with Ag ions with a kinetic energy in the range of 18–54 MeV to fluences between 10^{13} and 10^{15} ions/cm^2 at 300 K. For example, under irradiation with 18 MeV Ag^{+4} ions to a fluence of 6.4×10^{14} ions/cm^2, the originally spherical nanoparticles of 15 nm diameter are shaped into prolate nanorods with a length of 40 nm and a width of 8 nm. An aspect ratio of the major to the minor axis of the nanorods of about 5.0 ± 0.4 at constant volume is achieved. Saturation of the variation of the aspect ratio is reached at a fluence of 8.7×10^{14} ions/cm^2. Irradiation of samples containing 15 nm Au particles with 25 and 54 MeV Ag ions has shown further lengthening of the Au nanorods, increasing with the increasing ion energy. Similar ion-shaping behavior is reported for 30 nm Au particles under irradiation with 18, 25, and 54 MeV Ag ion energies, respectively. By systematically monitoring the experimental data, we put in evidence the existence of a threshold fluence of Au nanoparticle elongation. The value of the threshold fluence is found to depend on both the ion energy and nanoparticle size.

Keywords: ion beam, electronic stopping, Au nanoparticles, ion track, nanorods, nanowires

1. Introduction

The use of ion beams as effective tools for changing the material properties has gained increasing interest during the past few decades. In particular, emphasis is given to ion implantation [1] and focused ion beam [2] processes which have received an enormous amount of attention in semiconductor technology applications.

When an ion penetrates a solid, it dissipates its kinetic energy in collisions with the target atoms. Ion implantation is performed in the energy regime where electronic stopping dominates the minimal sputtering mechanism. Implanted ion profile and the concentration of impurity atom are affected by sputtering. As the target material is being bombarded with energetic ions, some of the incident beam ions are implanted and retained in the target, while the surface that is exposed to the ion beam is simultaneously receding due to sputtering. Schematic diagram of the ion-solid interaction is illustrated in **Figure 1** (adopted from Nastasi et al. [3]). The basic mechanisms characterizing the interactions of ions with solids can be summarized as follows:

1. Nuclear energy loss. This is the main mechanism of energy losses at low ion velocities (kinetic energy, corresponding to ~1 keV/a.m.u.). The bombarding particle transfers its energy to the nucleus of the target atom in elastic collisions, which causes the atoms to be displaced from their equilibrium positions.
2. Electronic energy loss. This is the predominant mechanism of energy loss for fast ions (≥ 1 MeV/a.m.u.). In this regime the ions lose their kinetic energy by electronic excitation and ionization of target atoms.
3. Photon radiation. Stopping through photon generation becomes significant only at relativistic velocities (bremsstrahlung, transitional Vavilov-Cherenkov radiation).
4. Nuclear reactions. Nuclear reactions of the projectile ion and target atoms occur when the two collision partners have sufficient kinetic energy that the Coulomb barrier can be overcome

Taking into account the fact that most attention is paid to ion-induced structural changes of materials within nuclear and electronic energy loss regimes, we shall only discuss the two first mentioned mechanisms of the ion-matter interactions. A good approximation is the assumption that nuclear and electron energy losses are uncorrelated and can therefore be discussed separately and independently.

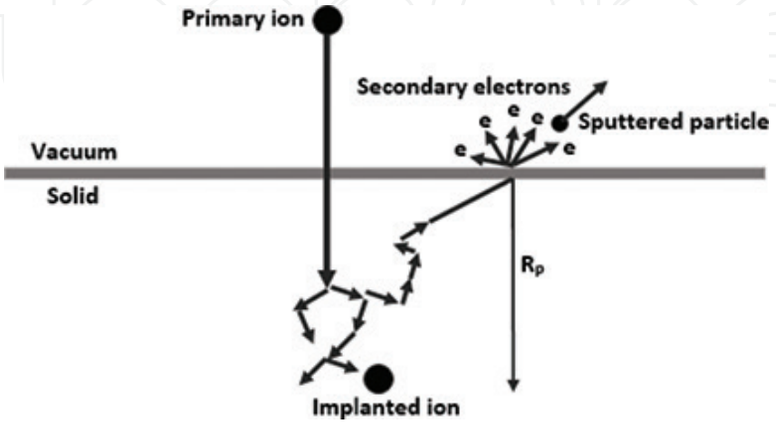

Figure 1. Schematic diagram of the ion solid interactions (adopted from Nastasi et al. [3]).

http://dx.doi.org/10.5772/intechopen.76862

In the case of nuclear stopping, elastic collisions cause the ions to change their velocity, but the total kinetic energy of the colliding atoms remains constant. On the other hand, inelastic collisions involving electrons are not accompanied by large changes in the direction of the ion, and here several processes are possible: excitation and ionization of atoms with electron exchange in the colliding atoms. A typical evolution of the energy loss as a function of the ion kinetic energy is presented in **Figure 2** for a beam of xenon ions (Xe ions) in amorphous SiO_2. From the figure, one can, for instance, infer that the electronic stopping power for an energy of 370 MeV is more than two orders of magnitude larger than the nuclear stopping power.

1.1. Ion beam-induced deformation

i. Anisotropic plastic deformation of colloidal silica particles

Heavy ions with ~MeV/a.m.u. kinetic energy predominantly lose their energy in a solid target material by electronic excitation and ionization of the target atoms. It is now well established that during irradiation with such ions, amorphous materials are subject to irreversible anisotropic changes of their specimen dimensions [4, 5]. Detailed description of the mechanism governing the anisotropic deformation is reported by the viscoelastic model. The latter presumes the deposition of energy by the incident ion into the electronic subsystem of the material. Through electron–phonon coupling, this energy is transformed in a cylindrical molten-like transient heating around the path of the particles. In a very short time interval (few femtoseconds), and as a result of the cylindrical molten expansion, shear stress relaxation induces freezing anisotropic stress as cooling of the heated regions is taking place. In this way,

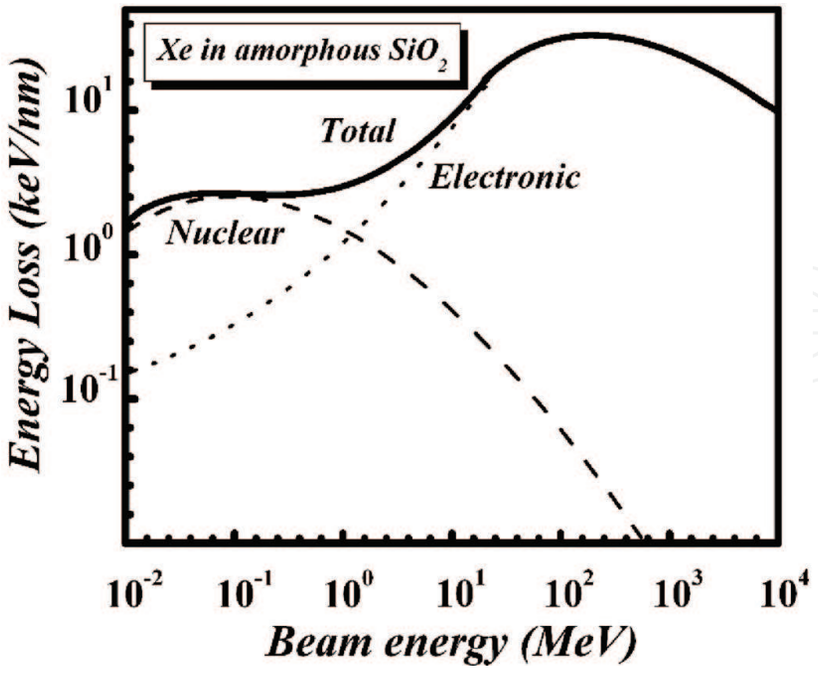

Figure 2. Nuclear, electronic, and total energy loss versus the ion energy for typical ion energy of 370 MeV Xe in amorphous SiO_2. The figure is reproduced with permission from M. Toulemonde [8].

the deformation mechanism is governed by electronic energy loss and most efficiently with ions in the MeV/a.m.u. energy range. Extrapolation of experimental high-energy to lower-energy data has suggested that the deformation is not expected to occur below a minimum irradiation energy of 1 MeV [6, 7]. The concept of the thermal spike is generally invoked to interpret the damage induced in amorphous materials such as metallic or silica glasses when they are traversed by ions with a kinetic energy in the electronic stopping regime.

ii. Anisotropic plastic deformation of embedded metal nanoparticles

Metal nanoparticles (NPs) are subject of large scientific and technological interest because of their specific properties which are different from those of the corresponding bulk material [9, 10]. When light impinges on (nano)-metal, the free conduction electron clouds respond collectively by oscillating in resonance, which excitation is known as a surface plasmon (SP). For a number of (noble) metals, the resonance behavior is noticeable in a single band in the visible range of the electromagnetic spectrum. One of the interesting aspects is the possibility to shift the surface plasmon resonance (SPR) peak of metal NPs into the infrared region by modifying their aspect ratio [11]. The SPR peak characteristics depend on the size, the shape, and the chemical environment of the metal NP; thus, modification of one of these parameters represents a way to control the optical properties of the material containing the NPs. In this respect, the ion beam-shaping technique is becoming a powerful tool to manipulate matter at the nanometer scale, allowing spherical dielectric particles to be transformed into prolate nanostructures, i.e., to elongate in direction perpendicular to the incident beam direction. Meanwhile, metal NPs embedded within a dielectric matrix are transformed into nanorods and/or nanowires that are aligned along the direction of the incident ion beam [12]. The latter is becoming an increasing scientific interest specially in tailoring the optical properties of plasmonic-active materials which could be widely used in applications within nanophotonics and nanoplasmonics [13].

2. Method

Compared to conventional surface science techniques, such as gas-phase synthesis and deposition of NPs under ultrahigh-vacuum condition, the self-assembly of NPs by means of electrostatic coupling is a scientifically and economically interesting alternative [14]. In the following, charge-stabilized spherical colloidal gold NPs, which have been derivatized with (3-aminopropyl)triethoxysilane (APTES), are deposited on the surface of thermally grown silicon oxide substrates. The thickness of the thermal oxide amounts to 200 nm. Two sets of samples with the different NP size of 15 and 30 nm diameter are prepared. Dispersion in size is deduced from atomic force microscopy (AFM) technique. AFM analysis of the particle heights is measured and found to amount to about ±3 nm. Each set consists of a number of identically prepared samples for each NP size.

At present AFM is one of the important techniques for analysis of surface morphology [15, 16]. The size and shape of Au NPs have been inspected by a Nanoscope® IIIa tapping mode atomic force microscope (TM-AFM) operating in air. **Figure 3** shows AFM images of Au NPs, distributed on the sample surface after immersion for 5 minutes into a solution containing Au NPs

http://dx.doi.org/10.5772/intechopen.76862

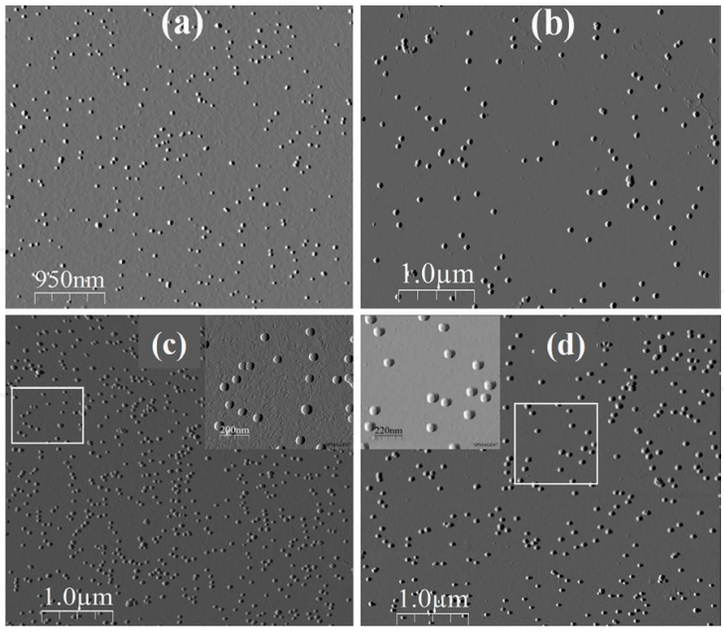

Figure 3. AFM images of 15 and 30 nm Au particles deposited on the SiO_2 surface after immersion into Au solution for 5 minutes, (a) and (b), respectively, and 40 minutes, (c) and (d), respectively.

with 15 and 30 nm diameter (a) and (b), respectively, and after immersion for 40 minutes into Au solution containing 15 and 30 nm diameter NPs, (c) and (d), respectively. These AFM images which were taken before sputter deposition of the second oxide layer show the uniformity of the Au NP distribution over the surface of the samples.

A silicon dioxide layer with thickness of about 150 nm is reactively sputtered to cover the Au NPs. Subsequently, the layer structure is annealed at 900°C in an open furnace. To provide a good thermal contact during the irradiation treatment, the samples are mounted on a massive copper holder using conductive paste. For better understanding of ion energy and NP initial size dependence, irradiations with 18, 25, and 54 MeV Ag ions are performed on the first set of the samples. This first set is composed of three identically prepared NPs of 15 and 30 nm diameter each. The additional set of samples composed of the same NP size is prepared at higher NP areal density as to investigate the role of NP density within the resulting deformation characteristics of embedded NPs. The variation in Au NP areal density is established by variation of the immersion time of the samples into the Au-containing solution, between 5 and 40 minutes. The resulting density of the 15 and 30 nm Au NP samples obtained following the deposition scheme between 5 and 40 minutes is estimated in **Table 1**. The average interparticle distance is calculated based on a square array of particles. The ion beam is electrostatically scanned to homogeneously irradiate the entire sample area of 2 × 2 cm. Irradiations are performed at room temperature (300 K) for fluences ranging from 10^{13} to 10^{15} ions/cm^2 applying normal incidence. Beam currents are sufficiently stable during irradiations as measured on a spot of 1 mm^2 using a micro-Faraday cup. The beams are delivered by the Utrecht 6.5 MV EN tandem accelerator. The values for the electronic stopping powers in SiO_2 and the projected range of the silver ions in SiO_2 at the energies applied are deduced from the SRIM program [17] and shown in **Table 2**.

Deposition time (±1 min)	5 minutes	10 minutes	20 minutes	30 minutes	40 minutes
15 nm Au NP concentration (particles/cm^2) (±10%)	2.5×10^9	7.5×10^9	1.4×10^{10}	1.7×10^{10}	4×10^{10}
Interparticle distance (±10 nm)	200	115	85	76	50
30 nm Au NP concentration (particles/cm^2) (±10%)	—	9×10^8	2.3×10^9	2.8×10^9	3.2×10^9
Interparticle distance (±10 nm)	—	333	208	188	176

Table 1. NP concentration and the corresponding interparticle distance of Au NPs with average size of 15 and 30 nm diameter deposited on SiO_2 substrate by immersion of the substrate into colloidal Au-containing solution for time intervals of 5, 10, 20, 30, and 40 minutes.

These ranges are far beyond the thickness of the oxide layers containing the metal nanoparticles. Hence, the irradiation is only used to deposit energy into the SiO_2-Au layers. The Au nanoparticle size and shape before and after irradiation are studied by using (tapping mode) atomic force microscopy (AFM), Rutherford backscattering spectrometry (RBS), and transmission electron microscopy (TEM).

Analysis of the samples has been carried out by different techniques. Rutherford backscattering spectrometry (RBS) is used to measure the density of Au species as it penetrates into the SiO_2 matrix. With respect to the latter, RBS is regarded as a faster tool to bring information about Au NP depth distribution before and after irradiation with heavy ion beams. The depth distribution of the Au NPs is estimated from the corresponding full width at half maximum (FWHM) of the Au peak in the RBS spectra. It is worth mentioning that under swift heavy ion (SHI) irradiation, the vast majority of the Au species will not be confined to their NPs due to melting; therefore, the FWHM of the Au peak cannot bring qualitative estimation of the exact NP size. However, a qualitative trend of the NP elongation can be followed. RBS analysis was carried out applying an incident $^4He^+$ ion beam with energy of 2 MeV at normal incidence geometry. The backscattered ions were analyzed in situ using two detectors at angles of 120° and 170°, respectively. In the "Results" section, we will only discuss the data analysis obtained from one detector of our selection (120° detector), assuming that the data obtained from the 170° are essentially identical. After RBS analysis, samples containing the metal NPs are analyzed by transmission electron microscope (TEM) for cross-sectional imaging of the size and shape of Au NPs before and after irradiation. For that purpose, a 300 keV Philips/CM30 microscope is used. The micrographs obtained from X-TEM analysis are processed with a slow scanning camera applying digital micrograph program.

	S_e (SiO_2) (keV/nm)	S_n (SiO_2) (keV/nm)	S_e (Au) (keV/nm)	S_n (Au) (keV/nm)	R_p (μm)
18 MeV^{+4}	5.4	0.23	11	0.9	5.8
25 MeV^{+5}	6.7	0.18	14	0.7	6.9
54 MeV^{+8}	9.7	0.10	24	0.4	10.3

Table 2. Values for electronic (S_e) and nuclear (S_n) stopping power for SiO_2 and gold and projected range (R_p) obtained for the applied ion beams (18, 25, and 54 MeV Ag ions). All the values are obtained using the code SRIM 2008 [17].

3. Results

Au NPs with average size of 15 and 30 nm diameter are prepared with different NP concentrations and/or areal densities (10^8–10^{10} particles/cm^2) embedded within a single plane parallel to the surface of a SiO_2 matrix. In this section, we will report a detailed investigation of swift heavy ion irradiation effects on these NPs. A selective range on incident ion energy of 18, 25, and 54 MeV Ag ions is applied. Influence of the ion energy, NP size, and areal density on the process of ion-induced elongation of spherical Au NPs will be discussed. For clarity of presentation, the "Results" section is divided into two subsections. The first subsection discusses the role played by embedded NP size and ion energy within the deformation characteristics at almost constant NP areal density and/or concentration. For that purpose, NP size range between 15 and 30 nm diameter is selected of which its samples are identically prepared and successively irradiated with ion beam energies in the range of 18–54 MeV Ag ions. In the second subsection, for the two NP sizes, the ion beam-induced deformation is investigated considering two extreme regions of NP areal density (low concentration and high concentration) applying single ion energy of 54 MeV Ag^{+8} ions.

3.1. Elongation as a function of the initial NP size and the ion beam energy

3.1.1. Evolution of 15 nm Au NPs

The first set consisting of three identically prepared samples, containing 15 nm Au NPs with an average areal density amounting to $1.7x10^{10}$ particles/cm^2, is irradiated with 18, 25, and 54 MeV Ag ions, respectively. **Figure 4a–c** shows the Au RBS peak as obtained from the 120° detector for several fluence values for the three energies. The relatively sharp peak of the unirradiated regions corresponds to 15 nm particles which are embedded in a SiO_2 matrix in a plane at a depth of approximately 150 nm below the surface. RBS analysis in **Figure 4a–c** shows broadening in Au NP peak with increasing the irradiation fluence. The broadening in the Au RBS peak indicates that the depth distribution of the Au is penetrating into the hosting SiO_2 matrix. The latter indicates that the pristine Au NP is transformed into aligned nanorods parallel to the ion beam direction. The evolution of the FWHM with fluence from the 120° and 170° detectors is shown in **Figures 5(a)** and **5(b)**, respectively.

From inspection of the data in both figures, two facts are deduced for irradiations of 15 nm Au NPs with 18 and 25 MeV Ag ions, as follows:

- **i.** No elongation appears for fluences lower than ~5.0×10^{13} and 3.0×10^{13} ions/cm^2, respectively.
- **ii.** The RBS peak width reaches saturation for fluences larger than ~$6–8 \times 10^{14}$ and 4.5×10^{14} ions/cm^2, respectively.

The X-TEM micrographs in **Figure 6a**, **b** correspond to the highest 18 MeV irradiation fluence (8.7×10^{14} ions/cm^2). Clearly, under 18 MeV Ag^{+4} ions, the originally spherical NPs of 15 nm diameter are all shaped into prolate nanorods with a length of ~40 nm and a width of ~8 nm, thus, with an aspect ratio of about 5. The volume of each nanorod corresponds approximately

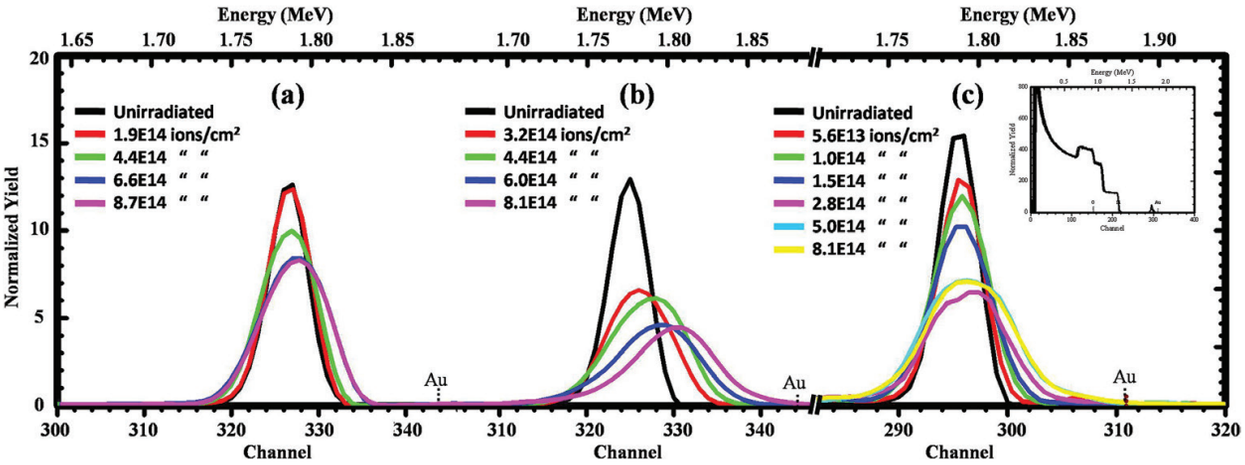

Figure 4. Normalized RBS spectra of three identically prepared samples containing Au NPs with 15 nm diameter with an average areal density of $1.7x10^{10}$ particles/cm^2 after being irradiated with energies of 18 MeV Ag^{+4} ions, 25 MeV Ag^{+5} ions, and 54 MeV Ag^{+8} ions, (a), (b), and (c), respectively. The inset shows total normalized spectra for all samples. The Au surface channel is indicated. The scale is (a), and (b) is the same; however, for (c), the experimental condition is slightly different.

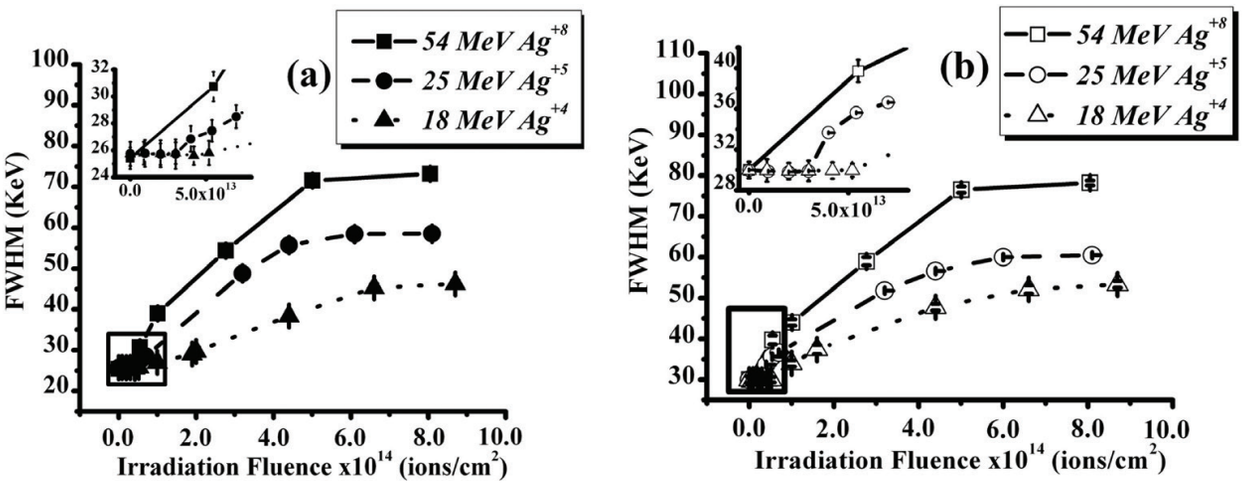

Figure 5. The FWHM of the Au peak as function of irradiation fluence determined simultaneously for the 120° and 170° scattering angles, (a) and (b), respectively. The figures are for 15 nm Au NPs irradiated with 18 MeV Ag^{+4} ion energy (triangles and dot line), 25 MeV Ag^{+5} ion energy (circles and dash line), and 54 MeV Ag^{+8} ion energy (squares and solid line). A magnified view of the region identified by the black square and the black rectangle is included in the inset of figure (a) and (b), respectively.

to that of the pristine spherical NP (V_{NR}~V_{NP}). This indicates that the ion-shaping process for these irradiation conditions is an individual process, i.e., each NP deforms into a similar prolate nanorod.

The broadening of the Au RBS peak for the sample irradiated with 54 MeV Ag^{+8} ions is also represented in **Figure 5a**, **b**. At this energy the elongation of 15 nm Au particles starts without detectable threshold fluence in these measurements. After irradiation to a fluence of 1.0×10^{14} ions/cm^2, the broadening of the Au RBS peak has already reached the value attained under irradiation with 18 MeV Ag^{+4} ions to the maximum fluence of 8.7×10^{14} ions/cm^2. The latter observation confirms the influence of the ion energy on the elongation characteristics of Au NPs.

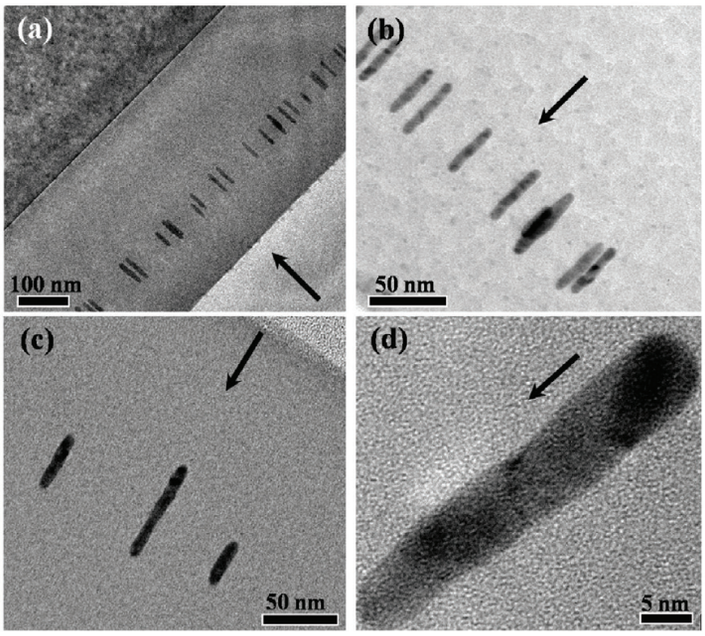

Figure 6. High-resolution X-TEM images of (i) 15 nm Au NPs under 18 MeV Ag^{+4} ions to a fluence of $8.7x10^{14}$ ions/cm^2 (a) and (b). (ii) 15 nm NPs under 54 MeV Ag^{+8} ions to a fluence of 1.0×10^{14} ions/cm^2 (c) and (d). The direction of the ion beam is indicated by the black arrows.

Strikingly, X-TEM micrographs corresponding to the irradiation with 54 MeV Ag^{+8} ions to a fluence of 1.0×10^{14} ions/cm^2 reveal almost similar nanorod morphology as those given in **Figure 6a**, **b**. These micrographs are given in **Figure 6c**, **d** showing aligned Au nanorods of approximately 40 nm length and ~8 nm width parallel to the ion beam direction. With increasing the irradiation fluence above 1.0×10^{14} ions/cm^2, the Au RBS peak continues to broaden until its width becomes constant for fluences larger than 5.0×10^{14} ions/cm^2.

3.1.2. Evolution of 30 nm Au NPs

A second set of three identically prepared samples containing 30 nm Au NPs with a areal density of about 2.8×10^9 particles/cm^2 are irradiated with 18, 25, and 54 MeV Ag swift heavy ions. The series (a–c) in **Figure 7** represents the evolution of the Au RBS peak with irradiation fluence at these energies. **Figure 8** shows the change in FWHM with fluence derived from the RBS spectra for the three energies using the 120° detector. From the figure, two facts are deduced similar to the case for 15 nm Au NPs under irradiations with 18 and 25 MeV Ag ions, as follows:

i. Elongation threshold fluences are observed, amounting to about $7.0x10^{13}$ and $5.0x10^{13}$ ions/cm^2, respectively.

ii. Saturation in FWHM of the Au RBS peak is reached at fluences $6.0x10^{14}$ and $5.0x10^{14}$ ions/cm^2, respectively.

For irradiation with 54 MeV Ag^{+8} ions, the ion-shaping effect starts again without detectable threshold fluence. At the same time, no saturation is visible up to a fluence 2.0×10^{14} ions/cm^2.

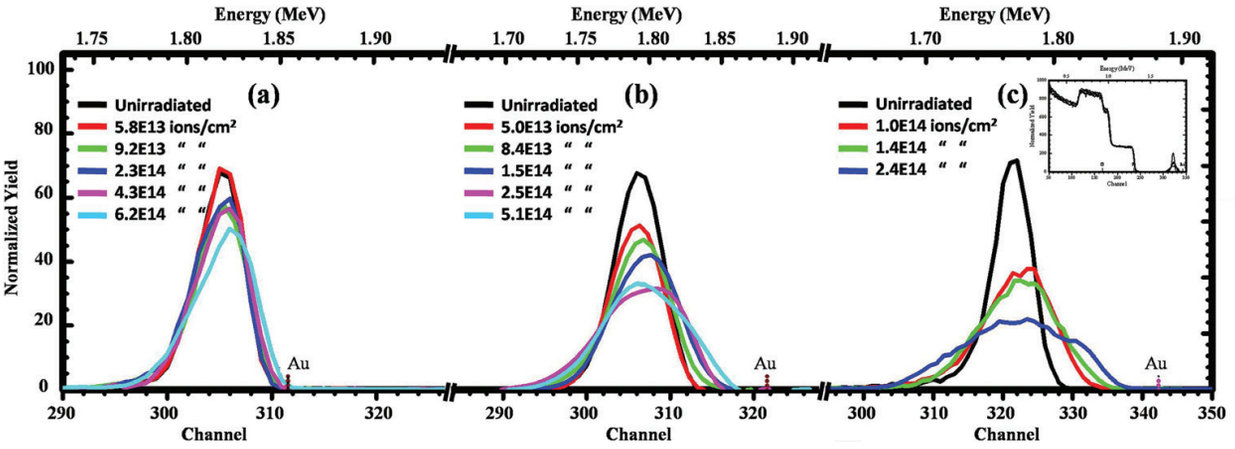

Figure 7. Normalized RBS spectra of 30 nm Au particles under (a) 18 MeV Ag^{+4} ions, (b) 25 MeV Ag^{+5} ions, and (c) 54 MeV Ag^{+8} ions for samples prepared with an average areal density of 2.8×10^9 particles/cm^2.

AFM analysis in **Figure 3** points to a good uniformity of Au NP distribution over the surface and the absence of agglomeration, i.e., clustering of individual NPs. This allows us to investigate the role of interparticle distance on the ion-shaping mechanism. Thus, in the following subsection, we will focus on the elongation phenomenon by varying the initial areal density of the Au NPs.

3.2. Elongation as a function of the initial NP size and initial NP concentration

3.2.1. Evolution of 15 nm Au NPs

Samples containing spherical Au NPs with diameter of 15 nm prepared with areal density between 0.25 and 4×10^{10} particles/cm^2 were irradiated with 54 MeV Ag^{+8} ions. The series

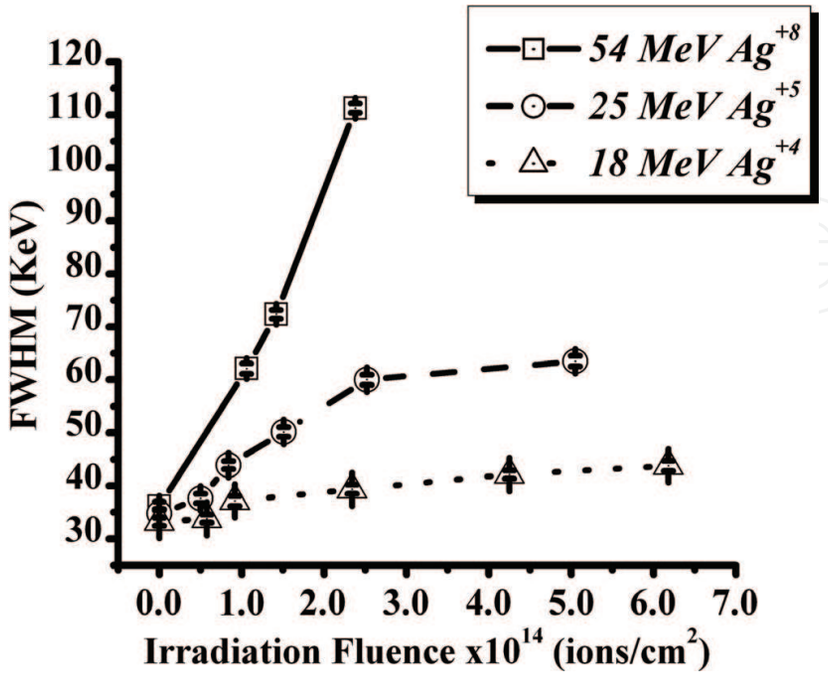

Figure 8. The relative change of Au peak width determined for the 120° scattering angle as a function of fluence for 30 nm Au particles under irradiation with 18 MeV Ag^{+4} ions (triangles and dot line), 25 MeV Ag^{+5} ions (circles and dash line), and 54 MeV Ag^{+8} ions (squares and solid line).

http://dx.doi.org/10.5772/intechopen.76862

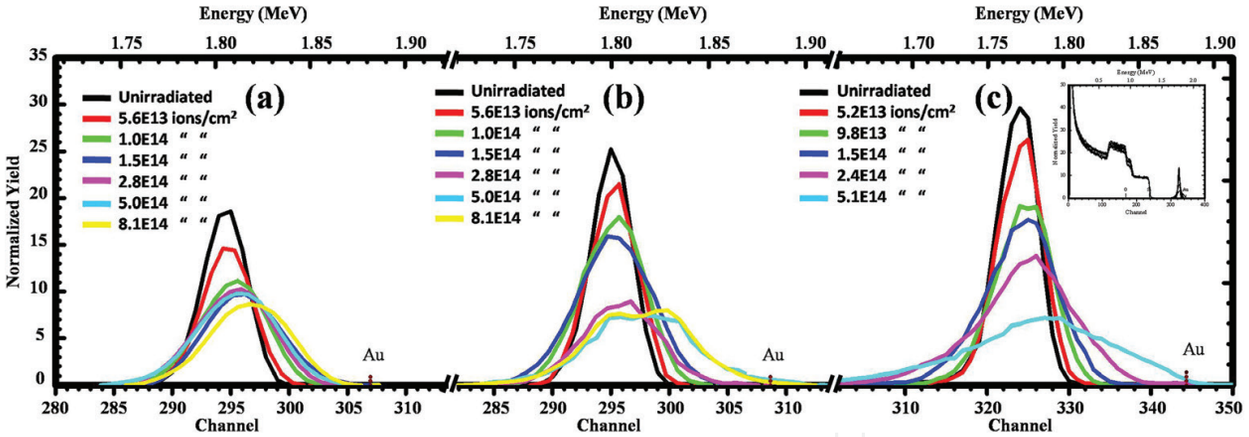

Figure 9. The Au RBS peak of 15 Au NPs for various irradiation fluences of 54 MeV Ag^{+8} ions for different areal densities of 2.5×10^9, 1.4×10^{10}, and 4×10^{10} particles/cm^2, (a), (b), and (c), respectively. Normalized RBS spectra are presented in the inset of plot (c).

(a–c) in **Figure 9** show the 15 nm Au RBS peak for various fluences for NP at areal density of 2.5×10^9, 1.4×10^{10}, and 4×10^{10} particles/cm^2, respectively. **Figure 10** shows the evolution of the FWHM of the RBS Au peak as a function of the fluence, for various values of the areal density. From the inspection of the figure, two regions clearly appear as follows: (i) For low irradiation fluences, the relative broadening of the RBS peak is almost the same for all samples irrespective of their areal density. We define this region as A. (ii) Above a critical fluence of about $1–2 \times 10^{14}$ ions/cm^2, the broadening of the RBS peak becomes significantly a function of the NP areal density. This region is denoted as region B. Apparently, all the curves tend to evolve toward a saturation value. The larger the initial NP areal density, the larger the saturation value of the FWHM appears to be.

We presume that in region A, Au NPs elongate into nanorods conserving their original volume ($V_{NR} \sim V_{NP}$). This is confirmed by X-TEM analysis as is shown in **Figure 11a–d**. To understand correlations between NP areal density and/or concentration and the broadening within the Au RBS peak observed in region B in **Figure 10**, we have selected two X-TEM micrographs of extreme NP densities (lower/higher) for comparison. As for the lowest NP density of 2.5×10^9 particles/cm^2, TEM micrographs in **Figure 11a**, **b** which correspond to irradiation fluence of 8.0×10^{14} ions/cm^2 is shown. The X-TEM micrograph in this figure shows aligned Au nanorods with major to minor axes of 100.8 nm. Calculation of the corresponding volume of these nanorods indicates that the volume for each nanorod is about twice the volume of the original pristine NP ($V_{NR} \sim 2V_{NP}$). Then, we consider the TEM micrographs corresponding to the highest areal density (4×10^{10} particles/cm^2) at a fluence of 5.0×10^{14} ions/cm^2 (see **Figure 11**). These micrographs are given in **Figure 11c–e** and show long nanowires with their major axis varying from 150 to 180 nm and minor axis of 8 nm. It is obvious that these wires are not the result of the deformation of a single particle because their Au content exceeds that of the initial NPs by at least a factor of 5 to 6, i.e., $V_{NR} \sim (5–6)\ V_{NP}$. We attribute that multiple Au NPs must have contributed to the growth of such nanowires. Seemingly, under swift heavy ion irradiation, some NPs deliver their species by disintegration, and through lateral transport, the disintegrated particles contribute to the growth of other particles. In this way, further lengthened nanostructures will appear in account of shorter ones. The latter hypothesis has been confirmed by X-TEM analysis where we observed smaller aligned particles, likely resulting from the fragmentation of some

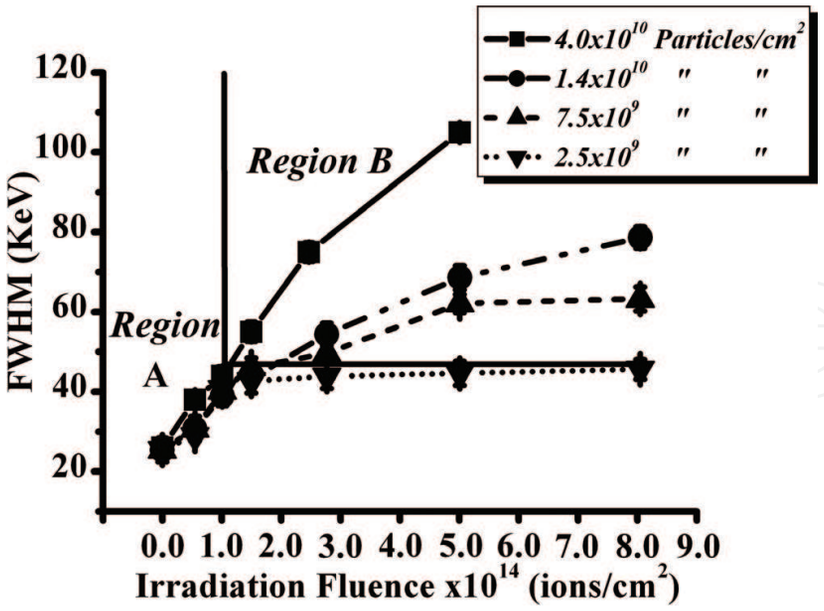

Figure 10. The FWHM of Au RBS peak obtained from the 120° detector as a function of 54 MeV Ag^{+8} irradiation fluence for different areal densities of 15 nm Au particles.

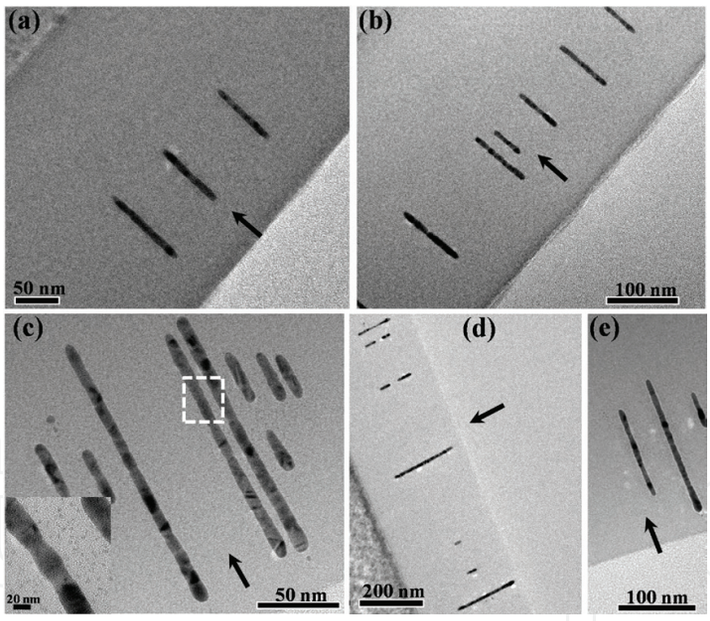

Figure 11. HR-XTEM images of (i) 15 nm Au particles with initial areal density of about 2.5×10^9 particles/cm^2 after irradiation with 54 MeV Ag^{+8} ions to a fluence of 8.1×10^{14} ions/cm^2, (a) and (b), respectively. (ii) 15 nm Au particles with an initial areal density of 4.0×10^{10} particles/cm^2 irradiated with 54 MeV Ag^{+8} ions to a fluence of 5.0×10^{14} ions/cm^2, (c), (d), and (e), respectively. The direction of the ion beam is indicated by the black arrows.

ion-deformed nanorods or nanowires. It emerges that the variation of NP areal density, and the concomitant variation of the interparticle distance, results in a strong variation in the shaping characteristics of the spherical Au NPs. For the areal density larger than 2.5×10^9 particles/cm^2

http://dx.doi.org/10.5772/intechopen.76862

and above the critical fluence of 1.0×10^{14} ions/cm^2, Au NPs start to disintegrate, while others continue to grow by accumulation of atoms and/or fragments from the disintegrating particles. The latter is assumed to occur by means of a process that is well known as Ostwald ripening. Interestingly, in some regions of TEM micrographs, tiny satellite particles surrounding shorter particles were seen (inset of **Figure 11c**). These satellite particles were not visible before irradiation. It is clear that the relative increase in Au peak width of the lowest areal density sample has already attained its maximum value just above the critical fluence. This might imply that there exists a threshold areal density for nanowire formation for 15 nm diameter Au particles, at an areal density of ~5.0×10^9 particles/cm^2, under 54 MeV Ag^{+8} ion irradiation. This corresponds to an interparticle distance of about 150 nm. Presumably, the mass transport process is effectively limited by a too large distance between the Au NPs.

3.2.2. Evolution of 30 nm Au NPs

Au NPs having an average diameter of about 30 nm and areal density ranging between 0.9 and 3.2×10^9 particles/cm^2 were irradiated with 54 MeV Ag^{+8} ions up to a fluence of 5.0×10^{14} ions/cm^2. The Au RBS peaks and the evolution of the FWHM of Au peak with the fluence for each NP areal density are shown in **Figure 12a–c** and **Figure 13**, respectively.

Again, we report the existence of two separated regions as in **Figure 10**. At lower irradiation fluences, the Au NP broadening evolves the NP size (region A). However, for fluences larger than a certain value (estimated for this NP size of about 1.0 x 10^{14} ions/cm^2), the broadening in Au NPs in region B evolves the NP areal density. As can be seen in **Figure 14a**, **b**, X-TEM micrographs show Au nanowires of a length of about 150~200 nm and a width of 8 nm aligning as a result from irradiation of the 30 nm Au NPs with areal density of 3.2×10^9 particles/cm^2 with 54 MeV Ag^{+8} ions to a fluence of 5.0 x 10^{14} ions/cm^2 (see **Figure 3.5**). From the data in this figure, we deduce a threshold interparticle distance near 250 nm for nanowire formation, i.e., at an areal density of approximately 9.0 x 10^8 particles/cm^2.

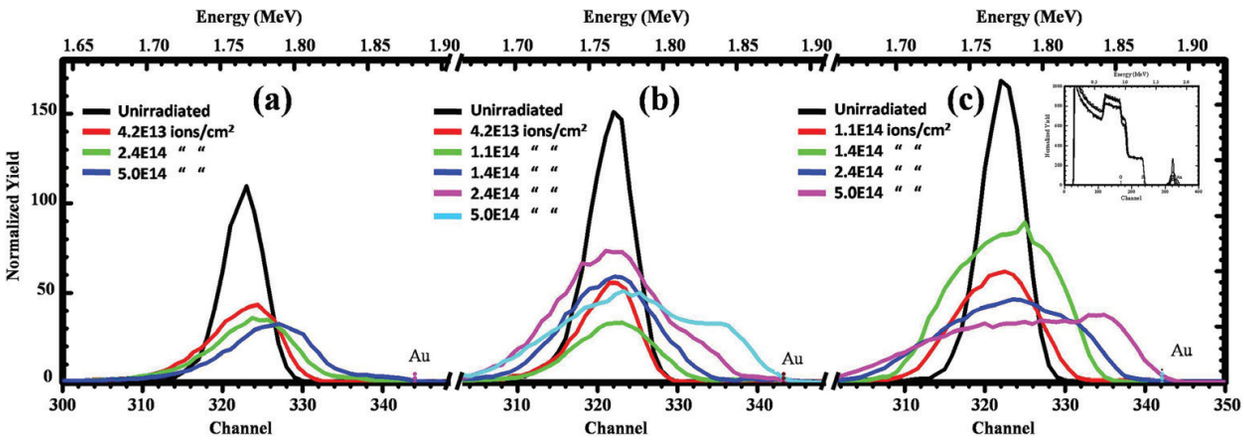

Figure 12. The Au RBS peak of 30 Au NPs for various irradiation fluences of 54 MeV Ag^{+8} ions for different areal densities of 9.0×10^8, 2.8×10^9, and 3.2×10^9 particles/cm^2, (a), (b), and (c), respectively. Normalized RBS spectra are presented in the inset of plot (c).

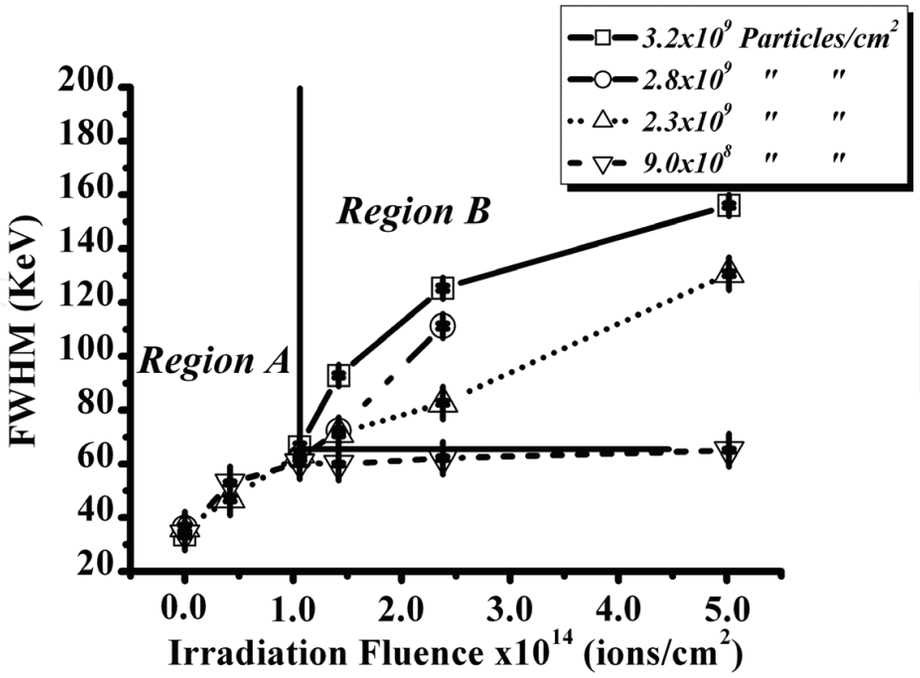

Figure 13. The FWHM of Au RBS peak obtained from only the 120° detector as a function of 54 MeV Ag^{+8} irradiation fluence for different areal densities of 30 nm Au particles.

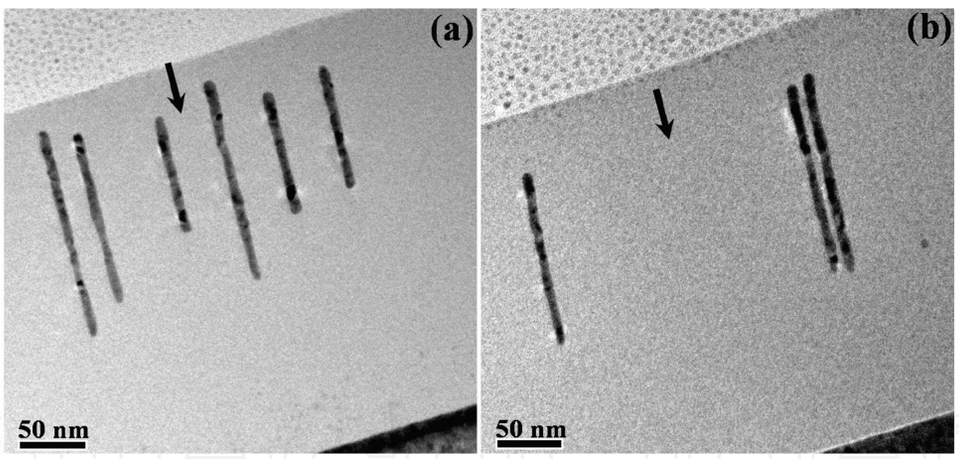

Figure 14. HR-XTEM images of 30 nm Au particles with initial areal density of 3.2×10^9 particles/cm^2 irradiated with 54 MeV Ag^{+8} ions to a fluence of 5.0×10^{14} ions/cm^2, (a) and (b), respectively. The direction of the ion beam is indicated by the black arrows.

4. Discussion

As pointed out in the experimental section, the projected ranges of the ions at the applied energies are far beyond the location of the spherical Au NPs. Thus, the elongation of such metal NPs must be a result of the ion passage through the SiO_2-Au-containing layer.

Systematic investigations of the deformation of NPs in response to swift heavy ion (SHI) irradiation have allowed us to evidence experimentally the existence of a threshold fluence for elongation, Φ_c. The threshold fluence for elongation as a function of ion energy and NP size

for 15–80 nm Au particles is estimated in **Table 3**. The value of Φ_c has been observed to depend on both ion energy and pristine NP size. In particular, Φ_c decreases with increasing electronic stopping power and increases with the NP diameter. However, as suggested by Klaumünzer [18, 19] and successively experimentally shown by Penninkhof et al. [20, 21], irradiation-induced NP elongation is a complicated issue where both the matrix and the characteristics of the confined NPs play an active role. Here, we put forward three possible mechanisms that could be the origin of the existence of a threshold fluence and its variation with NP size and incident ion energy. These mechanisms are listed as followed:

i. Preparation methodology of the samples.

ii. The compaction of the hosting silica matrix under irradiation.

iii. Occurrence of the irradiation-induced stresses within the silica matrix constrained by a substrate.

iv. Following the process at which our samples are prepared, Au NPs are first assembled on top of a thermally grown SiO_2 film and subsequently confined by sputtering of a secondary layer of SiO_2 that is reactively sputtered on top of the first layer. The final configuration of the active region of the samples indicates that Au NPs are embedded in a single plane 200 nm far from the surface of the sample. Chemically, gold is known to have a fairly poor wetting affinity with the SiO_2. Consequently, the mechanism of how precisely the oxide layer is formed around the Au NP during the deposition process is basically unknown. Following the process, our SiO_2 top film is grown at zone 1 at the low adatom mobility growth mode [22] and relatively low ion bombardment energy [23]. Within this sputtering scheme, most likely voids will form near the lower half of the NP in the growing oxide. The latter is attributed due to shadowing effects. On the other hand, during X-TEM analysis, none of the aforementioned voids were imaged. Therefore, it is plausible that a certain compaction of the SiO_2 surrounding the NP is required before the deformation process is activated.

v. It has been mentioned in literature that under irradiation with swift heavy ions at low fluences, the SiO_2 matrix exhibits a compaction of about 3%. At higher irradiation fluences, an anisotropic growth dominates the compaction phase [24–27]. Rearrangement of the SiO_2 ringlike material into smaller compact ring volume leads to densification of the silica matrix [28, 29]. For swift heavy ion irradiation, within each individual cylindrical ion track, the virgin material density is irreversibly modified. Subsequent ion impact within the same region does not produce any further density changes [24]. In this view, the fluence required to achieve

Ion energy	Nanoparticle size (nm)	Threshold fluence (ions/cm^2)
18 MeV Ag^{+4}	15	5×10^{13}
25 MeV Ag^{+5}		3×10^{13}
18 MeV Ag^{+4}	30	7×10^{13}
25 MeV Ag^{+5}		5×10^{13}

Table 3. The threshold fluence for elongation as a function of ion energy and NP size for 15–80 nm Au particles.

the compaction corresponds slightly to a compromise where all incident neighboring tracks exhibit mutual overlap in such way that the perturbed area covers the overall sample surface.

vi. As mentioned in our experimental part, our grown silica film is not free standing films but constrained by underneath silicon substrate. The stress state of a constrained silica film as an effect of the ion irradiation has been intensively studied in literature [25–27]. Two extremely opposite stress situations depending on the irradiation fluence have been reported as follows: (1) under irradiation at low ion fluences, the initially compressive stress turns into a tensile stress. The latter, which is related to the mechanism of compaction, leads to the structure to a higher equilibrium density state. The maximum value for this equilibrium is reached at the end of the matrix densification for fluences up to few 10^{13} ions/cm^2. (2) Under irradiation with fluences larger than 10^{14} ions/cm^2, anisotropic material deformation becomes quiet prominent in the further evolution of the system. The latter effect is associated with the tensile stress reduction and the buildup of a compressive stress for the constrained film.

Considering mechanisms (i) and (ii), we presume that the NP elongation is limited to the accomplishment of the structural transformation of the silica matrix. With the latter in mind, we try to correlate the threshold deformation evolution with the energy of the incident ions. As the end of SiO_2 matrix compaction implies the situation whereas the sample surface becomes entirely covered by the mutually overlapping ion tracks, it is conceivable that the resulting deformation threshold depends on the incident ion track diameter. In that sense, the larger the track radius is, the lower the deformation threshold fluence will be. In literature, a number of experimental and theoretical publications have already reported on the ion track cross sections in SiO_2 matrix [30–33]. In these publications, the track size is calculated from the thermal spike model and already found to correspond to the region that melted in the wake of the passing heavy projectile [34]. In our current results, the applied ion energies of 18, 25, and 54 MeV Ag, the corresponding electronic stopping powers in SiO_2 amount to 5.4, 6.7 and 9.7 keV/nm). The corresponding track diameters for these energies in the silica are approximately 3, 4, and ~5 nm, respectively. The calculated corresponding complete overlap of the ion tracks at the surface of the sample is found at fluences of 2.0×10^{13}, 1.0×10^{13}, 0.7×10^{13}, and 0.5×10^{13} ions/cm^2, respectively.

Putting on mind that (i) the swift heavy ion irradiation follows random statistics and that (ii) the compaction fluence for a silica matrix containing partially wetted metallic NP can be different from that of pure silica film, our calculations account pretty well for the reported reduction of the deformation threshold when the incident ion energy is increased.

In our results, we show that the inertia against NP elongation increases with size. In other words, NPs with larger diameters require higher electronic stopping powers to be deformed. Since the macroscopic stress induced by heavy ion irradiation in planar constrained films can reach larger values (several hundreds of MPa) [26], we presume that that mechanism (iii) can actively participate in deformation process of the embedded Au NPs. The aforementioned scenario of (iii) has already been introduced by Roorda et al. [12] for verification of the shape change of Au NPs confined within a silica shell and suggested to remain solid during the irradiation. However, this indirect mechanism alone is not enough to correlate the observed deformation of embedded solid NPs [18]. The metallic NP must have an active participation in the elongation process. In other words, the elongation process will only take place when

the temperatures of both the metallic NP and the surrounding dielectric matrix exceed their individual melting temperatures [18, 19]. In literature, it has been argued that the melting of metallic NPs with diameters in the range of nearly similar range to our NPs of the current study (6 and 20 nm) cannot be invoked with energy deposition corresponding to the electronic stopping powers in the current work [35]. Particles with relatively larger diameters are not expected to completely melt and virtually are not observed to deform under SHI irradiation, [18, 35, 36]. Awazu et al. [35] report that Au NPs with diameter of about 50 nm are not subject to deform under irradiation with 110 MeV Br ions to a fluence of about 1.0×10^{14} ions/cm^2. For this class of NP size, it is conceivable that a minimum compressive stress is needed to activate the NP deformation. On the other hand, it is necessary to mention that the threshold fluence cannot be directly regarded to the individual track-generated stress [37–39]. This is because the deformation threshold would be only dependable on the electronic stopping. Consequently, macroscopic stress should be invoked to clarify the observations. In this sense, direct correlation between minimum compressive stress and NP size could be established. The larger NP size requires larger (minimum) compressive stress to activate the NP elongation process leading to larger fluence necessary to reach it. The latter hypothesis accounts quiet well for our results for the deformation dependence on initial NP size, ion energy, and irradiation fluence. Furthermore, the variation of the embedded NP areal density has led to identification of two distinct fluence regimes for the NP elongation under swift heavy ion irradiations as follows:

i. For low irradiation fluences, Au NPs deform into ion beam-aligned nanorods. This morphology transformation occurs under volume conservation. In other words, the ion-shaping mechanism is an individual mechanism, where each pristine NP deforms into a single oblate nanorod. As this behavior is observed for all values of the NP areal density, in this first stage which is represented by the region A, the ion-shaping process can be seen as an *individual process* as far as the nanoparticles are concerned.

ii. For irradiation fluences above—somewhat critical threshold—of 1.0 x10^{14} ions/cm^2, RBS analysis indicates that the deformation rate is sensitive to the initial NP areal density. With increasing the NP areal density, the deformation rate increases. In this deformation's secondary stage, high-resolution TEM images show long Au nanowires aligned in direction of the ion beam accompanied by strong signs of Au disintegration and/or fragmentation. As the volume of the longer nanowires visualized is about five to six times the volume of the originally spherical NP, the NP elongation process in this fluence-dependent region necessitates the contribution of several individual nanostructures. Within this fluence region, the elongation process might be identified in terms of a *collective process* where some of already-deformed NPs, or even some of the aligned nanowires, dissolve under the irradiation, while other nanowires continue to grow by integration of the atoms from the dissolving particles. The mechanism behind the driving force identifies which nanowire should dissolve and which nanowire should grow remain unknown. Consequently, there is a need for more detailed experimental and theoretical approach to verify it.

The mechanism governing the growth of Au nanowires most likely involves the diffusion through the silica matrix of the gold solute from the dissolved/fragmented nanoparticles toward the growing ones. The task to identify the physical origin of the driving force for preferred Au diffusion from shorter Au nanorods to longer ones, which causes a kind of Ostwald ripening, is difficult.

Some insights can be obtained from **Figure 11(c)** (the inset) and **Figure 14a**, **b** where small fragments are clearly visualized. In fact, those small fragments were not imaged before irradiation; thus, they must be a product of the ion beam irradiation. The energy deposited within the NP subsystem may have allowed the Au atoms and/or species to dissolve in silica. Upon local fluctuation of the solute concentration, the supersaturation of the solid solution then evolves toward the precipitation of the satellite particle phase. Under swift heavy ion irradiation, these small precipitates become unstable [40], and thus they dissolve by subsequent impinging ions (track by track) through the silica matrix. In other words, the diffusion of such nanostructures is driven by the transient melted region formed in the wake of the impinging ions. Dais et al. [41] report on direct observation of the gold diffusion within the ion track. As this process depends on the amount of the available solute sources, i.e., the NP concentration, the lower their relative distance the shorter the diffusion time and the longer the nanowires, as shown in **Figure 13c**, **d** and **Figure 14a**, **b**. On the other hand, when the NP areal density is low, the particle growth is limited by the too long distance between the metal particles. This effect accounts for the relatively low saturation length observed in the samples having the lowest NP areal density. If metal solute may diffuse only within the thermal spike region, for each ion impact, the lateral diffusion distance will be of the order of magnitude of the track size. In the current study, the calculated ion track radius corresponding to the applied ion energies ranges between 3 and 5 nm. Considering the minimum calculated interparticle distance of NPs of about 50 nm, and assuming that the minimum fluence needed for the sample surface overlap is about 1.0×10^{13} ions/cm^2, approximately ten ion impacts within the region are necessary to diffuse over 50 nm. Therefore, the minimum fluence required for solute metal atoms to diffuse from one particle to the nearest one is about 1.0×10^{14} ions/cm^2. The latter accounts quiet well with the fluence necessary to pass from the individual deformation region (*denoted as A*) to the collective deformation process region (*denoted B*) in our results.

Thus, the possibility to grow Au nanowires under swift heavy ion irradiation requires basically the possibility for original NPs to deform and the availability of short-distance solute sources to achieve an effective mass transport. It seems further required that the particles have a certain nanorod shape before the nanowire region is entered or that, alternatively, a certain fluence is applied to enter this region. For Au NPs larger than 30 nm diameter, the mechanism governing nanowire creation requires greater total energy deposition than the value applied here. We note a tendency that the elongation rate diminishes at a higher nanorod length for a higher areal density. For Au NPs of 15 and 30 nm diameter and with increasing irradiation fluence, the minor axis of the elongated nanorods reaches a saturated width at 8 nm. Much in standing with, Giulian et al. [36] report on the elongation process of Pt NPs with size of about 7 nm diameter in a SiO_2 matrix. In this study, the minor axis of the elongated Pt NPs is found to reach a saturation at an increasing fluence, while the saturation value of the minor axis increases with increasing the incident in energy. The latter is attributed due to the NP confinement within a well-defined molten track radius in the amorphous SiO_2 matrix. On the other hand, Pt NPs with size smaller than 7 nm diameter did not show any sign of deformation but mostly indicate a decrease in size as a result of dissolution. In addition, Au nanocrystals (NCs) [42] with size between 1 and 6 nm diameters further grow in size under SHI irradiation with 100 MeV Au^{+8} ions to fluences of 5×10^{12} and 2×10^{13} ions/cm^2. These Au NCs were produced by implantation of 4×10^{16} ions/cm^2 of the 32 keV Au ion into silica glass. With increasing the irradiation fluence to 1×10^{14} ions/cm^2, the amount of Au nanocrystals retained in the silica matrix dropped to about 20% of its initial value as a result of dissolution. These observations

suggest that smaller NPs have the tendency to fragmentation and/or disintegration. With the latter in minds, a hypothesis could be that when the minor axis of the aligned nanostructures (nanorods and/or nanowires) is reaching a critical value (maybe in the order of about 8 nm), such nanostructures will disintegrate under subsequent direct ion impact. Due to the parallelism of such nanostructures with the ion beam direction, such ion impact does immediately affect the entire nanowire. Besides, a minimum value for the minor axis of the nanorods and/or nanowires implies that these aligned nanostructures can only be further elongated when atoms from the matrix are collected. In additions, the mutual ion impacts determine which nanowires disintegrate and which grow. In this frame, the NP disintegration and growth are treated as a continuous process, extending also in the region of the collective growth (region B). Eventually, and in view of the decreasing density of the nanowires, the rate of disintegration with fluence decreases and so does the rate of elongation until ultimately a saturation length is reached.

5. Conclusion

In this chapter, we have shown that the shape of originally spherical Au NPs embedded in a single plane within a SiO_2 matrix can be modified by swift heavy ion irradiations. Under Ag swift heavy ion irradiation, spherical Au NPs undergo anisotropic deformation into single prolate nanorod with their long axis parallel to the ion beam direction. Systematic experimental investigation has led to the existence of the so-called threshold fluence for deformation. The extent of the latter has been carried out by variation of both NP size and ion energy. In addition, we have shown that the NP size and areal density have a substantial influence on the characteristics of the ion-induced elongation of confined NPs. In that respect, a well-defined size-dependent NP elongation below a certain irradiation fluence (region A) is identified. In this region, all the NPs elongate following *individual elongation process* depending only on NP size. Under irradiation with fluence above a certain critical value of 1.00×10^{14} ions/cm^2, region B at which the deformation is regarded as *collective mechanism* is defined. In this region, longer nanowires are created as a product of several metallic NP contribution to the nanowire growth. Furthermore, in region B, the NP deformation increases with increasing initial NP areal density, i.e., the higher the initial NP areal density is, the longer the nanowires are grown.

Author details

Elmuez A. Dawi

Address all correspondence to: e.dawi@ajman.ac.ae

Ajman University, Ajman, UAE

References

[1] Mayer JW. Ion implantation in semiconductors. Electron Devices Meeting, 1973 International, 1973; Vol. 19. pp. 3-5

[2] Cheam DD, Bergstrom PL. ASC manuscripts. 2008; M/MP-2

[3] Nastasi M, Mayer JW, Hirvonen JK. Ion-Solid Interactions: Fundamentals and Applications. Great Britain: Cambridge University Press; 1996

[4] Klaumünzer S, Schumacher G. Physical Review Letters. 1983;**51**(1987)

[5] Klaumünzer S, Ming-dong H, Schumacher G. Physical Review Letters. 1986;**57**(850)

[6] Benyagoub A, Löffler S, Rammensee M, Klaumünzer S, Saemann-Ischenko G. Nuclear Instruments and Methods in Physics Research Section B. 1992;**65**(228)

[7] van Dillen T, Polman A, Fukarek W, van Blaaderen A. Applied Physics Letters. 2001; **78**(7):910

[8] Toulemonde M, Dufour C, Meftah A, Paumier E. Nuclear Instruments and Methods in Physics Research Section B. 2000;**903**:166-167

[9] Gerardy JM, Ausloos M. Physical Review B. 1982;**25**:420

[10] Penninkhof JJ, Polman A, Sweatlock LA, Maier SA, Atwater HA, Vredenberg AM, Kooi BJ. Applied Physics Letters. 2003;**83**(20):4137

[11] Quinten M, Kreibig U. Applied Optics. 1993;**32**:6173

[12] Roorda S, van Dillen T, Polman A, Graf C, van Blaaderen A, Kooi BJ. Advanced Materials. 2004;**16**:235

[13] Gonella F, Mazzoldi P. Handbook of Nanostructured Materials and Nanotechnology. Vol. 4. San Diego: Academic Press; 2000

[14] Kooij ES, Brouwer EAM, Wormeester H, Poelsema B. Colloids and Surfaces A: Physicochem. Engineering Aspects. 2003;**222**:103

[15] Zhong O, Inniss D, Kjoller K, Elings VB. Surface Science Letters. 1993;**290**:L688

[16] Digital Instruments, Santa Barbara, CA

[17] Ziegler JF, Biersack JP, Ziegler MD. SRIM–A version of the TRIM program, The Stopping and Range of Ions in Matter (2008). Available from: http://www.srim.org

[18] Klaumünzer S, et al. Nuclear Instruments and Methods in Physics Research Section B. 2006;**244**:1

[19] Klaumünzer S, et al. Nuclear Instruments and Methods in Physics Research Section B. 2004;**225**:136

[20] Penninkhof JJ, Graf C, Van Dillen T, Vredenberg AM, Van Blaaderen A, Polman A. Advanced Materials. 2005;**17**:1484

[21] Penninkhof JJ. PhD Thesis. Utrecht University, September, 25th (2006)

[22] Messier R, Venugopal VC, Venul PD. Journal of Vacuum Science and Technology. 2000; **A 18**:1538

[23] van Hattum ED, Palmero A, Arnoldbik WM, Rudolph H, Habraken FHBM. Applied Physical Letters. 2007;**91**:171501

[24] Benyagoub A, Klaumünzer S, Toulemonde M. Nuclear Instruments and Methods in Physics Research Section B. 1998;**146**:449

[25] Snoeks E, Weber T, Cacciato A, Polman A. Applied Physics. 1995;**78**:4723

[26] Brongersma ML, Snoeks E, van Dillen T, Polman A. Journal of Applied Physics. 2000;**88**:59

[27] van Dillen T, Siem MYS, Polman A. Applied Physics Letters. 2004;**85**:389

[28] Primak W. Studies in Radiation Effects in Solids Gordon and Breach. Vol 4. New York; 1975

[29] Devine RAB. Nuclear Instruments and Methods in Physics Research Section B. 1994;**91**:378

[30] Meftah A, Brisard F, Constantini JM, Dooryhee E, Hageali M, Hervieu M, Stoquert JP, Studer F, Toulemonde M. Physical Review B. 1994;**49**:12457

[31] Meftah A, Djebara M, Khalfaoui N, Toulemonde M. Nuclear Instruments and Methods in Physics Research Section B. 1998;**146**:431

[32] Kluth P, Schnohr CS, Sprouster DJ, Byrne AP, Cookson DJ, Ridgway MC. Nuclear Instruments and Methods in Physics Research Section B. 2008;**266**:2994

[33] Rotaru CC. Ph.D. thesis. University of Caen, 2004. Available from: http://tel.archives-ouvertes.fr/tel-00005399

[34] Toulemonde M, Dufour C, Paumier E. Physical Review B. 1992;**46**:14362

[35] Awazu K, Wang X, Fijimaki M, Tominga J. Physical Review B. 2008;**78**:054102

[36] Giulian R, Kluth P, Araujo LL, Sprouster DJ, Byrne AP, Cookson DJ, Ridgway MC. Physical Review B. 2008;**78**:125413

[37] Trinkaus H, Ryazanov AI. Physical Review Letters. 1995;**74**:5072

[38] Trinkaus H. Nuclear Instruments and Methods in Physics Research Section B. 1998;**146**:204

[39] Kluth P, Schnohr CS, Pakarinen OH, Djurabekova F, Sprouster DJ, Giulian R, Ridgway MC, Byrne AP, Trautmann C, Cookson DJ, Nordlund K, Toulemonde M. Physical Review Letters. 2008;**101**:175503

[40] D'Orléans C, Stoquert JP, Estournès C, Grob JJ, Muller D, Guille JL, Richard-Plouet M, Cerruti C, Haas F. Nuclear Instruments and Methods in Physics Research Section B.2004; **216**:372

[41] Dais C, Bolse T, Bolse W, Shubert-Bischoff P, Lindner JNK. Nuclear Instruments and Methods in Physics Research Section B. 2006;**245**:239

[42] Joseph B, Ghatak J, Lenka HP, Kuiri PK, Sahu G, Mishra NC, Mahapatra DP. Nuclear Instruments and Methods in Physics Research Section B. 2007;**256**:659

IntechOpen